JCBFM

Original Article

Quantification of the purinergic P2X7 receptor with [11C]SMW139 improves through correction for brain-penetrating radiometabolites

Joachim Brumberg[1,2] , Richard Aarnio[3] , Anton Forsberg[1],
Päivi Marjamäki[3], Vera Kerstens[1], Mohammad M Moein[1],
Sangram Nag[1], Saara Wahlroos[3], Michael Kassiou[4],
Albert D Windhorst[5,6], Christer Halldin[1],
Merja Haaparanta-Solin[3], Patrik Fazio[1,7], Vesa Oikonen[3],
Juha O Rinne[3] and Andrea Varrone[1]

Abstract

The membrane-based purinergic 7 receptor (P2X7R) is expressed on activated microglia and the target of the radio-ligand [11C]SMW139 for *in vivo* assessment of neuroinflammation. This study investigated the contribution of radio-labelled metabolites which potentially affect its quantification. *Ex vivo* high-performance liquid chromatography with a radio detector (radioHPLC) was used to evaluate the parent and radiometabolite fractions of [11C]SMW139 in the brain and plasma of eleven mice. Twelve healthy humans underwent 90-min [11C]SMW139 brain PET with arterial blood sampling and radiometabolite analysis. The volume of distribution was estimated by using one- and two- tissue compartment (TCM) modeling with single (V_T) and dual (V_{Tp}) input functions. RadioHPLC showed three major groups of radiometabolite peaks with increasing concentrations in the plasma of all mice and humans. Two radiometabolite peaks were also visible in mice brain homogenates and therefore considered for dual input modeling in humans. 2TCM with single input function provided V_T estimates with a wide range (0.10–10.74) and high coefficient of variation (COV: 159.9%), whereas dual input function model showed a narrow range of V_{Tp} estimates (0.04–0.24; COV: 33.3%). In conclusion, compartment modeling with correction for brain-penetrant radiometabolites improves the *in vivo* quantification of [11C]SMW139 binding to P2X7R in the human brain.

Keywords

[11C]SMW139 PET, dual input modeling, neuroinflammation, purinergic receptor, radiometabolite

Introduction

Inflammatory response to cerebral accumulation of misfolded proteins contributes to disease development of neurodegenerative diseases.[1,2] Microglia are the main immune cells of the central nervous system and detect changes in their cellular environment, provide physiological function, and promote tissue repair mechanisms.[3] Whereas initial microglial activation is assumed to have a beneficial effect, chronic and excessive stimuli may result in neuronal damage and thus, trigger the progression of neurodegeneration.[4,5]

[1]Centre for Psychiatry Research, Department of Clinical Neuroscience, Karolinska Institutet & Stockholm Health Care Services, Stockholm, Sweden
[2]Department of Nuclear Medicine, Medical Center – University of Freiburg, Freiburg, Germany
[3]Turku PET Centre, University of Turku and Turku University Hospital, Turku, Finland
[4]School of Chemistry, The University of Sydney, Sydney, Australia
[5]Department of Radiology and Nuclear Medicine, Amsterdam UMC location Vrije Universiteit Amsterdam, Amsterdam, The Netherlands
[6]Amsterdam Neuroscience, Brain Imaging, Amsterdam, The Netherlands
[7]Department of Neurology, Karolinska University Hospital, Stockholm, Sweden

Corresponding author:
Joachim Brumberg, Karolinska Hospital, R5:02 SE-17176 Stockholm, Sweden.
Email: joachim.brumberg@ki.se

The membrane-based purinergic, ligand-gated ion channel 7 receptor ($P2X_7R$) is an adenosine triphosphate (ATP)-gated, non-selective cation channel and is upregulated in activated microglia.[6–8] Whereas it physiologically has trophic actions on neurons, microglia, and astrocytes, it is activated by high ATP-levels after tissue injury, leading to the release of pro-inflammatory substances.[9] This triggers further microglial activation, promotes neuronal damage, and subsequent apoptosis, that induces a continued ATP-release and thus, sustains a vicious circle of neuronal inflammation and cell loss.[6] Due to its involvement in this cycle, the $P2X_7R$ is a promising molecular target to reveal the pathophysiologic mechanisms of neuroinflammation and for new therapeutic approaches.

Four radiolabeled adamantanyl benzamide analogues with high affinity to the human $P2X_7R$ have been evaluated in rodent animal models, of which [11C]SMW139 showed highest binding to the receptor.[10] The radioligand is not a substrate of the P-glycoprotein at the blood-brain-barrier (BBB) and uptake can be blocked with $P2X_7R$ antagonists.[11] [11C]SMW139 was evaluated in humans including the characterization of [11C]SMW139 pharmacokinetics.[12] However, the suggested kinetic model did not account for the possible presence of brain-penetrating radiometabolites of [11C]SMW139 as indicated by preclinical evidence.[10] Therefore, this study aims to extend previous findings on brain-penetrating radiometabolites by evaluating [11C]SMW139 metabolism preclinically and to assess whether kinetic modeling with dual (i.e. parent and radiometabolite) input functions improves the *in vivo* quantification of $P2X_7R$ expression in humans.

Materials and methods

Small animal study

Eleven C57BL/6J mice were examined with [11C]SMW139 (all female; weight: 34 ± 4 g; age: 8.7 ± 1.9 months; injected activity: 17.9 ± 6.2 MBq; molar activity: 42.2 ± 24.1 MBq/nmol; injected mass: 0.21 ± 0.12 µg; for radiochemistry see Supplemental methods [13,14]). *Ex vivo* sampling for parent fraction analysis was performed at 10 min ($n = 4$), 30 min ($n = 3$) and 45 min ($n = 4$) post radioligand injection (p.i.) by cardiac puncture and by collecting perfused brain samples. Sample size of $n \geq 3$ per group was considered sufficient for exploratory radiometabolite analysis. All experimental animal procedures were done in accordance with the EU Directive 2010/63/EU on the protection of animals used for scientific purposes, and with the ARRIVE guidelines at Turku PET Centre, University of Turku, Finland [TU] and approved by

the Regional State Administrative Agency for Southern Finland (ESAVI/16273/2019).

Blood and brain radiometabolite analysis. Blood samples were collected into heparinized tubes (Microtainer, BD, Franklin Lakes, NJ, USA) and centrifuged (12100 g, 90 s). The plasma pipetted into an Eppendorf tube and mixed with 1:2 (v/v) plasma:acetonitrile to precipitate the proteins. The mixture was vortexed for 10 s, centrifuged, and the supernatant (200–700 µL) was collected for subsequent radio detector high-performance liquid chromatography (radioHPLC) analysis. Obtained brains were homogenized in a glass homogenizer with a 9:1 (v/v) acetonitrile:water solution. The homogenized solution was centrifuged (12100 g, 90 s) and the supernatant (200–700 µL volume) was analysed with radioHPLC (see Supplemental methods).

Human study

Human participants were prospectively enrolled and examined at two study sites (TU and Centre for Psychiatry Research, Karolinska Institutet, Stockholm, Sweden, [KI]). The study was approved by the Ethics Committee of the South Western Finland Hospital District, the Finnish Medicinal Agency, the Ethics Committee of the Stockholm Region, and the Radiation Safety Committee of the Karolinska University Hospital. The study was registered as Clinical Trial in the EudraCT database (2017-001585-19). All human participants provided written, informed consent before participating in the study, which was conducted in accordance with the Declaration of Helsinki and its later amendments. Twelve healthy subjects (TU: seven, KI: five) were recruited through public advertisement. Inclusion criteria were: age between 45 and 80 years, good health according to medical and psychiatric history, physical examination, cognitive assessment (Mini-Mental State Examination ≥ 28), laboratory tests, electrocardiogram, and unremarkable magnetic resonance (MR) imaging of the brain.

Imaging procedures. All subjects underwent brain MR scans, including T1-weighted three-dimensional sequences on a 3 Tesla system prior to PET examination as part of the initial evaluation and to delineate anatomic brain volumes of interests (VOI). Six min transmission scans with a ^{137}Cs source and the dynamic PET measurements were performed on a High-Resolution Research Tomograph system (Siemens Medical Solutions) at both study sites. [11C]SMW139 (424.0 ± 54.8 MBq; 152.0 ± 131.5 MBq/nmol; 1.91 ± 1.31 µg) was injected as bolus into the cubital vein and the catheter was flushed with 10 mL 0.9% NaCl

solution. Following injection, emission data were collected in list mode for 90 min. PET data were reconstructed in 21 frames of increasing duration (3×5 s, 3×10 s, 4×60 s, 2×150 s, 2×300 s, 7×600 s) using 3D ordinary Poisson ordered subset expectation maximization (8 iterations, 16 subsets, voxel size of $1.22 \times 1.22 \times 1.22$ mm). Frame-to-frame co-registration of reconstructed images was applied as previously published.[15]

Image analysis. All data were processed at KI using an in-house pipeline written in MATLAB (MATLAB r2014b, The MathWorks, Inc.). Individual T1-weighted sequences were segmented with FreeSurfer (FreeSurfer v6.0.0, http://surfer.nmr.mgh.harvard.edu/).[16] The generated segmentation masks were used to define bilateral VOIs of the frontal cortex, parietal cortex, temporal cortex, caudate nucleus, putamen, thalamus, brainstem, cerebellar cortex, and the whole-brain grey matter. Thereafter, MR and dynamic PET data were co-registered and time-activity curves (TAC) of VOIs were obtained.

Arterial blood sampling, radiometabolite analysis, and data processing. A catheter was placed into the radial artery of each participant and arterial blood was collected continuously during the first 5-10 min using an automated blood sampling system (ABSS, Allogg AB). A series of arterial blood samples were drawn manually at $\sim$2, 5, 10, 20, 40, 60, 75, and 90 min p.i. (Supplemental Table 1). The radioactivity in blood and plasma samples (0.7–1.7 mL) were measured in a well counter cross-calibrated with the PET system. The fraction of unchanged [^{11}C]SMW139 (i.e. parent fraction) in arterial blood was measured using radioHPLC analysis. At TU, the same chromatographic method as described for the small animal studies was used. At KI, the plasma was precipitated after centrifugation utilizing a simple protein precipitation method[17] and the supernatant was analysed by a reversed-phase radioHPLC as previously described.[18] The radio-chromatograms for radioactive compounds were integrated and their areas were calculated as a percentage of the total of the decay corrected areas of all detected radioactive fractions. Blood data were processed as previously described with slight modifications to generate plasma TACs,[19] parent input of [^{11}C]SMW139, and one input curve representing the activity of presumably brain-penetrant [^{11}C]SMW139 radiometabolites in the plasma (see Supplemental methods).

Kinetic modeling. Three kinetic models were assessed to characterize [^{11}C]SMW139 kinetics using PMOD (version 3.7, PMOD Technologies LLC). All models were applied by fitting the blood volume (V_B) as an additional parameter.[12] First, standard two-tissue compartment model with a single (i.e. parent) input curve was assessed with a dual run procedure (2TSI[k_4]), for which the efflux rate from the specific to the non-specific compartment, k_4, was first estimated in the whole-brain grey matter VOI and then used to fix k_4 for subsequent volume of distribution (V_T) estimation in (sub-)cortical grey matter VOIs.[12] This resulted in four parameters estimated in the second run (V_B, K_1, k_2, k_3). Second, one- and two-tissue compartment models with dual (i.e. parent and radiometabolite) input curves were evaluated (1TDI and 2TDI).[20] This led to five parameters for 1TDI (V_B, K_{1p}, k_{2p}, K_{1m}, k_{2m}) and seven parameters to fit for 2TDI (V_B, K_{1p}, k_{2p}, k_3, k_4, K_{1m}, k_{2m}). In analogy to 2TSI[k_4], the dual input two-tissue compartment model was also assessed with a two-step procedure (2TDI[k_4]; six parameters: V_B, K_{1p}, k_{2p}, k_3, K_{1m}, k_{2m}). According to the models, the total distribution volumes[21] can be achieved by solving equation (1) for 2TSI, equation (2) for 1TDI, and equation (3) for 2TDI where V_{Tp} is the distribution volume of the unchanged radioligand. The models assumed that the brain-penetrant radiometabolites did not specifically bind to the P2X$_7$R, so that the rate constants k_3 and k_4 represent solely the association and dissociation of the parent radioligand to the receptor. For model overview see Table 1.

$$V_T = \frac{K_1}{k_2} \times \left(1 + \frac{k_3}{k_4}\right) \tag{1}$$

$$V_{Tp} = \frac{K_{1p}}{k_{2p}} \tag{2}$$

$$V_{Tp} = \frac{K_{1p}}{k_{2p}} \times \left(1 + \frac{k_3}{k_4}\right) \tag{3}$$

Table 1. Model overview.

Model	Abbreviation	Fitted parameters
Two tissue compartment model with single input function and fixed k_4	2TSI[k_4]	V_B, K_1, k_2, k_3
One tissue compartment model with dual input function	1TDI	V_B, K_{1p}, k_{2p}, K_{1m}, k_{2m}
Two tissue compartment model with dual input function	2TDI	V_B, K_{1p}, k_{2p}, k_3, k_4, K_{1m}, k_{2m}
Two tissue compartment model with dual input function and fixed k_4	2TDI[k_4]	V_B, K_{1p}, k_{2p}, k_3, K_{1m}, k_{2m}

Statistical analysis. The coefficient of variation (COV) was calculated to assess the variability of distribution volumes and obtained by dividing the standard deviation by the mean, of all regions and subjects. The goodness of fit was assessed with the Akaike information criterion (AIC) [22] and the reliability of V_T and V_{Tp} by using the percentage standard error (%SE) of the estimates. The fits of dual input models were compared by using F-test statistics. The correlations of V_{Tp} estimates were assessed by using linear regression analysis and

Spearman's correlation coefficient r_s. A p-value below 0.05 was considered significant. Data are presented as mean and standard deviation or median and range, as appropriate.

Results

Ex vivo *radiometabolite analysis*

There was no exclusion within the small animal study. RadioHPLC showed three major groups of
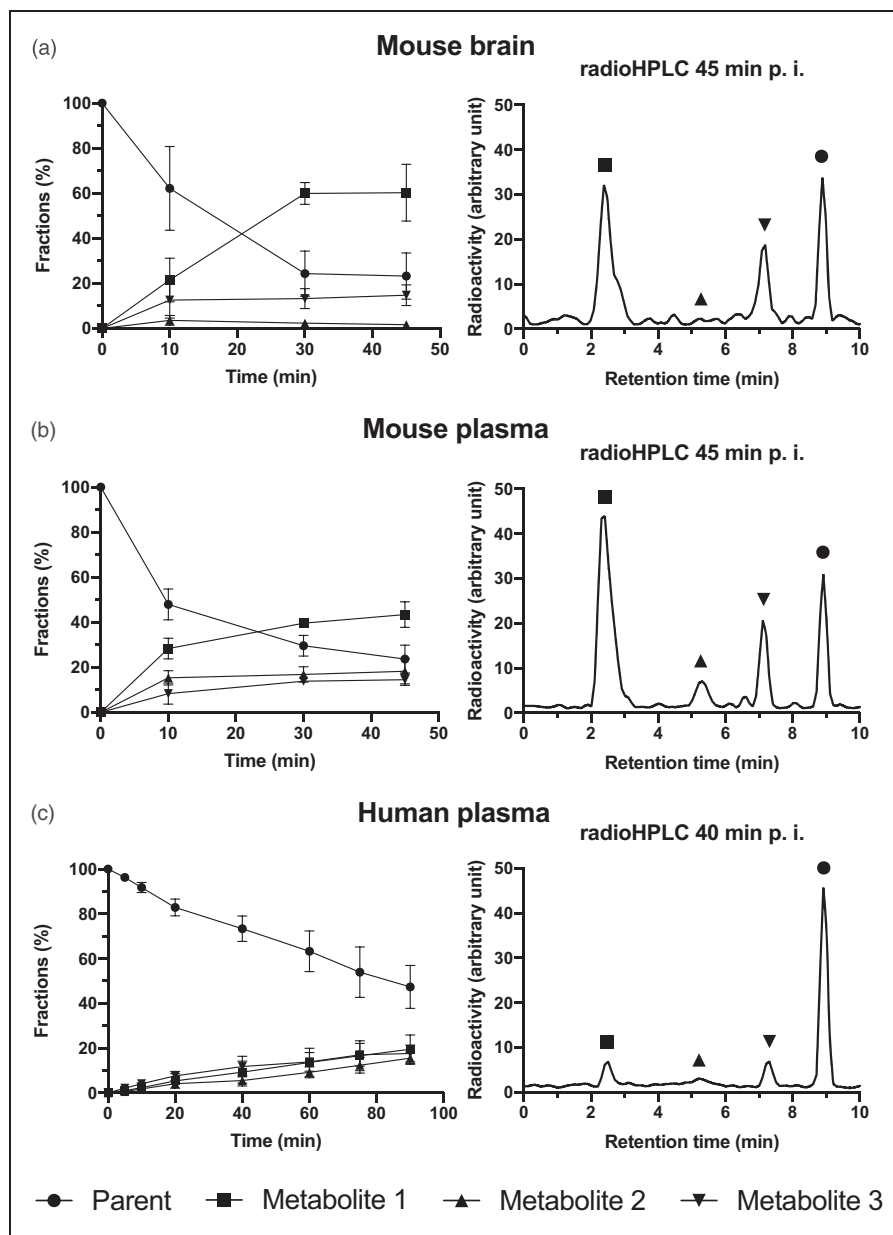

Figure 1. [^{11}C]SMW139 radiometabolite analysis. Left panels show mean and standard deviation of parent radioligand and radiometabolite fractions of the whole radioactivity in the sample in mouse brain (a) and mouse plasma (b) (n = 4, 3, and 4, at 10, 30, and 45 min, respectively), and human plasma (c; n = 10). Right panels show exemplary radioHPLC chromatograms from mouse (a, b) and human plasma (c).

radiometabolite peaks (numbered radiometabolite 1–3 according to the appearance order in radioHPLC chromatogram) with increasing concentrations over time in the plasma of all mice (Figure 1(b)). Only two peaks, the most polar radiometabolite 1 (retention time [Rt] 1.5–3.5 min) and the least polar radiometabolite 3 (Rt 7–8 min), were also clearly present in the mice's brain homogenates, whereas radiometabolite 2 (Rt 3.5–7 min) was only present in barely quantifiable levels (Figure 1(a)). The mean fraction of unchanged [^{11}C] SMW139 at 45 min after injection was similar in plasma and brain: around $23.7 \pm 6.2\%$ and $23.3 \pm 10.3\%$, respectively. A high fraction of radioligand metabolites after 10 min (plasma: $52.1 \pm 6.8\%$; brain: $37.8 \pm 18.6\%$) and an apparent transformation into a plateau phase in plasma and brain starting around 30 min p.i. indicates a much faster metabolism of [^{11}C]SMW139 in mice compared to humans (Figure 1).

Human plasma radiometabolites and brain uptake

Two subjects were excluded due to incomplete blood and plasma data. Plasma radioHPLC measurements showed three groups of radiometabolites peaking with an identical Rt when compared to mice plasma (Figure 1(c)). Human metabolism, however, was slower than that of mice yielding $47.3 \pm 9.6\%$ unchanged [^{11}C]SMW139 and continuing slightly increasing curves of all three radiometabolites fractions at 90 min p.i. (Figure 1(c)). Visual evaluations of TACs from the whole-brain grey matter showed that five subjects (50%; TU: two subjects, KI: three subjects), after the initial peak during the perfusion and uptake phase, had a clear washout of the tracer until the end of the scan. In contrast, the TACs of the remaining showed

a washout up to 20–40 min, followed by a slight and steady increase until the last frame (Figure 2).

Kinetic modeling

Tissue distribution volumes of single and dual input models.
Estimated distribution volumes and %SEs for each evaluated model is presented region-wise in Table 2. 2TDI yielded unstable fits with unreliably high V_{Tp} estimates and %SE > 50% in nine (11.3%) out of 80 evaluated regions (eight regions per patient). The observed fitting failures were equally distributed across regions and subjects without a particular VOI that performed poorly. Therefore, these regions were excluded from subsequent comparisons. 2TSI[k_4], 2TDI[k_4], and 1TDI yielded robust fits for all regions with predominantly low %SE < 20% except few outliers (Table 2). None of the regions were excluded. 2TSI [k_4] single input model showed a high COV of V_{T} (159.9%), whereas dual input models had a consistently narrow V_{Tp} range between 0.04 and 0.24 (COV: 2TDI, 33.3%; 2TDI[k_4], 36.3%; 1TDI, 35.0%; see also Figure 3). V_{B} estimates were in close agreement for all evaluated models (V_{B} [median, range]: 2TSI [k_4], 0.07, 0.02–0.13; 2TDI, 0.07, 0.02–0.13; 2TDI[k_4], 0.07, 0.01–0.13; 1TDI, 0.07, 0.02–0.13) with a consistently low %SE (median <3.5 for all models).

Model comparison.
Two tissue compartment models showed overall comparable ranges of AIC's with slight differences between regions. AIC was predominantly smallest for 2TDI[k_4]. Median AIC of 1TDI was tendentially higher than two tissue compartment models (Table 3). Median F-value of the comparison between 2TDI and 2TDI[k_4] was below the tabulated value at a p-level of 0.05 (F critical value: 4.60) for all
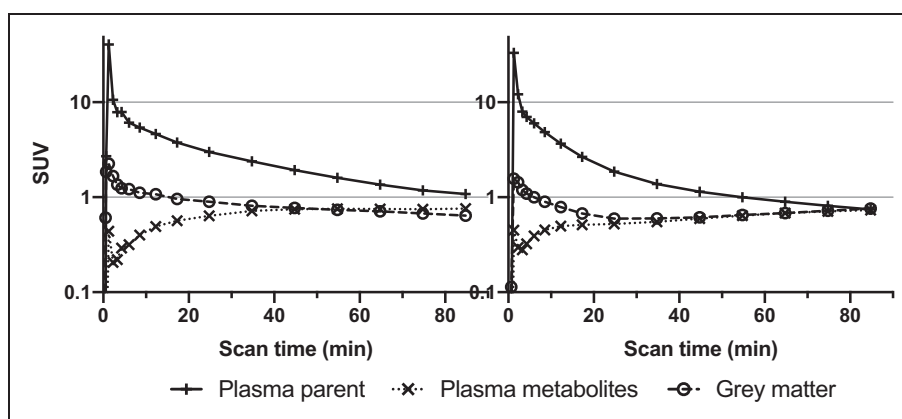

Figure 2. Human time-activity curves. Left panel shows an exemplary finding in one subject with initial peaking followed by washout from the whole-brain grey matter time-activity curves. Right panel shows an exemplary whole-brain grey matter time-activity curve with a slight and steady increase after 20–40 min. Both are depicted with corresponding plasma parent and plasma radiometabolite standardized uptake value (SUV) curves.

Table 2. Estimated tissue distribution volumes and percentage standard error.

Volume of interest	Two tissue compartment model, single input, k_4 fixed		Two tissue compartment model, dual input[a]		Two tissue compartment model, dual input, k_4 fixed		One tissue compartment model, dual input	
	V_T	%SE V_T	V_{Tp}	%SE V_{Tp}	V_{Tp}	%SE V_{Tp}	V_{Tp}	%SE V_{Tp}
Frontal cortex	0.58 (0.17–10.06)	4.4 (2.8–9.5)	0.14 (0.07–0.21)	8.3 (3.8–13.1)	0.13 (0.07–0.17)	4.9 (2.4–24.0)	0.09 (0.06–0.12)	5.8 (3.3–11.4)
Parietal cortex	0.71 (0.21–10.74)	3.9 (2.2–12.1)	0.15 (0.09–0.20)	13.4 (4.2–32.8)	0.14 (0.07–0.16)	5.5 (2.6–37.7)	0.09 (0.06–0.16)	6.5 (3.7–10.7)
Temporal cortex	0.53 (0.16–8.97)	3.8 (1.7–13.2)	0.13 (0.070.16)	5.9 (2.6–36.3)	0.14 (0.06–0.18)	5.4 (2.3–11.9)	0.10 (0.06–0.16)	4.4 (3.8–12.2)
Caudate	0.43 (0.10–7.24)	5.2 (4.0–7.9)	0.10 (0.04–0.14)	23.0 (6.9–40.4)	0.08 (0.04–0.16)	10.6 (3.5–17.1)	0.07 (0.04–0.12)	7.1 (3.2–20.4)
Putamen	0.61 (0.15–9.20)	6.2 (3.0–15.2)	0.14 (0.07–0.24)	13.6 (4.6–20.1)	0.15 (0.07–0.20)	9.2 (4.4–38.8)	0.10 (0.06–0.14)	6.1 (4.7–13.5)
Thalamus	0.53 (0.13–7.76)	5.5 (3.5–17.4)	0.16 (0.06–0.20)	6.3 (4.7–24.5)	0.14 (0.07–0.24)	6.0 (2.8–21.2)	0.11 (0.07–0.17)	5.4 (2.9–17.6)
Brainstem	0.41 (0.11–6.33)	4.7 (2.8–10.3)	0.14 (0.04–0.20)	9.7 (2.7–32.4)	0.14 (0.05–0.20)	8.3 (3.9–12.6)	0.11 (0.05–0.17)	5.9 (1.9–8.9)
Cerebellar cortex	0.51 (0.15–9.04)	5.0 (2.2–17.4)	0.13 (0.07–0.18)	13.3 (4.2–34.1)	0.11 (0.06–0.18)	5.5 (1.9–23.9)	0.09 (0.05–0.15)	5.0 (3.0–15.5)

Data of healthy volunteers (n = 10) are presented as median and range.
V_T: volume of distribution; V_{Tp}: distribution volume of unchanged radioligand; %SE: percentage standard error.
[a]Estimates of nine brain regions excluded.

eight brain regions, suggesting that the simplification of the 2TDI (i.e. using a dual run procedure to fix k_4) can be considered equivalent in terms of the model fit. However, when further simplifying the model to the 1TDI, median F-values are predominantly above the critical value (3.74), suggesting that the fit is significantly worsened and thus, this model does not completely describe the pharmacokinetics of $[^{11}C]$SMW139.

Correlation analysis

Linear regression showed that V_{Tp} estimates of all brain regions derived from 2TDI and 2TDI[k_4] ($r^2 = 0.74$, $p < 0.001$) as well as 2TDI[k_4] and 1TDI ($r^2 = 0.78$, $p < 0.001$) strongly correlated with each other, whereas the correlation between 2TDI and 1TDI ($r^2 = 0.64$, $p < 0.001$) was less pronounced (Figure 4). The same applied to each region separately which had high to excellent correlations (2TDI vs. 2TDI[k_4]: $r_s = 0.80$–1.00, all $p < 0.01$; 2TDI vs. 1TDI: $r_s = 0.70$–0.88, all $p < 0.05$; 2TDI[k_4] vs. 1TDI: $r_s = 0.81$–0.94, all $p < 0.01$; Supplemental Table 2).

Discussion

This study investigating $[^{11}C]$SMW139 metabolism in mice and pharmacokinetics in healthy human participants showed evidence that two $[^{11}C]$SMW139 radiometabolites are present in the brain and must be considered for accurate *in vivo* quantification of $[^{11}C]$SMW139 binding to the human P2X$_7$R. Kinetic modeling with plasma parent and radiometabolite input functions allows robust estimation of $[^{11}C]$SMW139 distribution volumes with low variability.

The P2X$_7$R is thought to have low expression levels in normal physiology and is upregulated in case of neuronal damage like in neurodegenerative disorders.[6,9] Since neurodegeneration is a chronic process, neuroinflammatory effects and regulatory mechanisms such as P2X$_7$R expression are expected to be subtle.[4,23] In this context, the correction for possibly confounding, brain-penetrant radiometabolites is of particular importance when evaluating tracers with low V_T values as it is the case for $[^{11}C]$SMW139.[12,20]

In our cohort of ten healthy volunteers, who were enrolled and examined at two different study sites, kinetic modeling with single input function yielded highly variable V_T estimates. Furthermore, V_T estimates in some cases were unexpectedly high and exceeded values that were previously reported with $[^{11}C]$SMW139.[12] Although the single input model showed robust fitting parameters, the fitted line undershot the late part of the TACs (Figure 3;[12]) suggesting that the assumption of $[^{11}C]$SMW139 radiometabolites
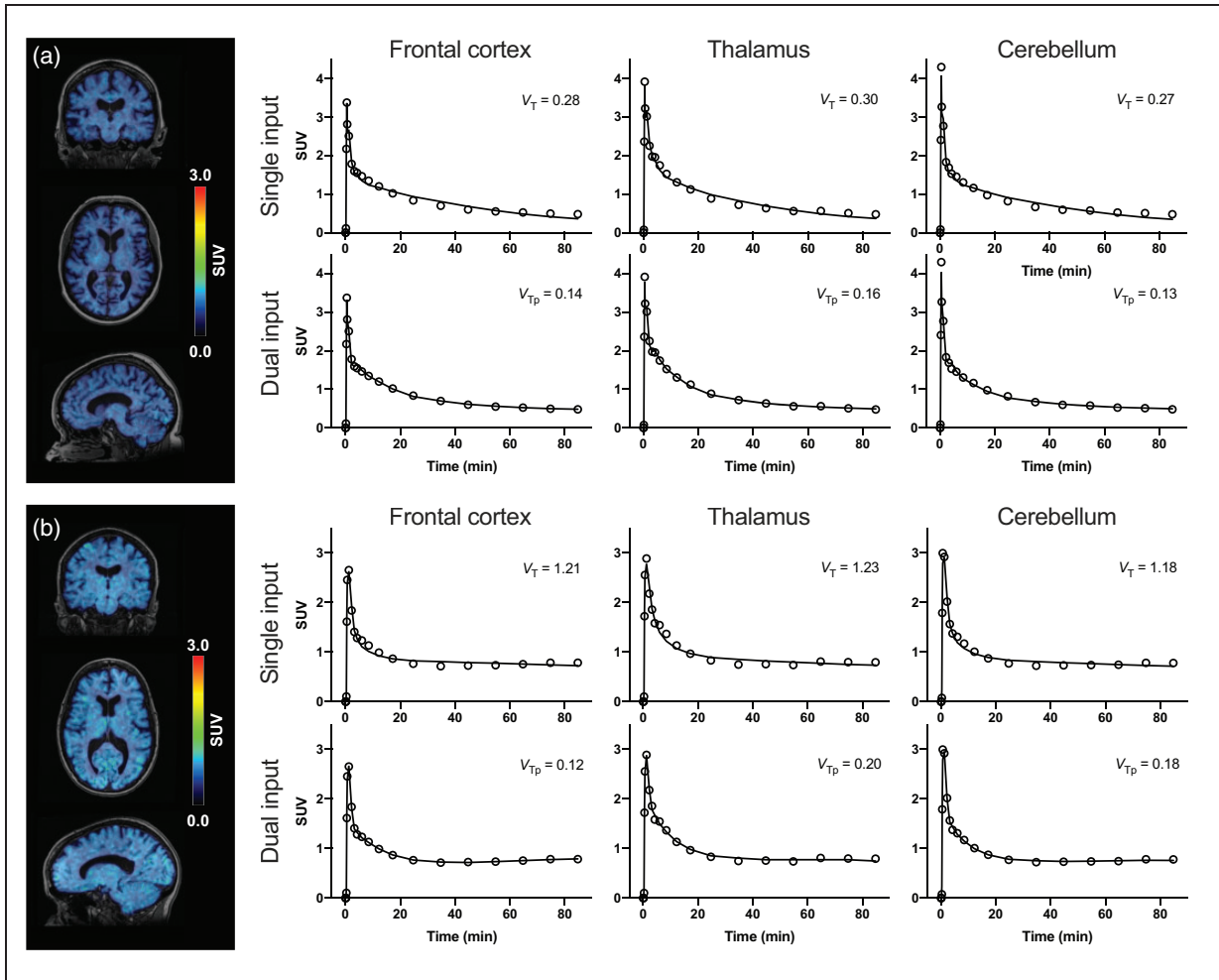
Figure 3. Two tissue compartment model fits with single and dual input function. Summarized standardized uptake value (SUV) images between 40 and 90 min after [^{11}C]SMW139 injection and exemplary model fits of two patients with low (a) and high (b) contribution of radiometabolites to brain radioactivity. Abbreviations: V_T, volume of distribution; V_{Tp}, distribution volume of the parent fraction.

not penetrating BBB in humans does not reflect the tracer's kinetics.

In the presence of three major groups of radiometabolites in the human plasma, however, it is unclear which radiometabolites may enter the brain and hamper the quantification of specific binding of [^{11}C]SMW139 to the P2X$_7$R. We, therefore, evaluated the [^{11}C]SMW139 metabolism in eleven C57BL/6J mice, in order to establish an analogy between humans and mice: considering a faster metabolism in mice as compared to humans,[24,25] the metabolization of [^{11}C]SMW139 is congruent by showing the three [^{11}C]SMW139 radiometabolites peaking with the same Rt (Figure 1). The most polar radiometabolite 1 and the least polar radiometabolite 3, were proven to be present in the brain of the mice, whereas radiometabolite 2 was detected only in low amounts in the examined perfused brain homogenates and showed in average

around 15% of the fraction levels found in plasma. Notwithstanding the state-of-the-art technique used in perfusion by pumping saline through blood vessels via the mouse's cardiac chambers after cardiac puncture, the brain may include small residuals of blood and thus, minor fractions of radiometabolite components in the plasma may affect the analysis of brain homogenates. This allows to disregard radiometabolite 2 for kinetic modeling assuming a similarly low ability to penetrate the human BBB.

Consecutively, we adjusted our assumptions for kinetic modeling by accounting for the presence of radiometabolite 1 and 3 within the human brain without specific binding to the P2X$_7$R. The variability of V_{Tp} estimates was reduced and the 2TDI fits were closer in agreement with the TACs (Figure 3). By reducing the number of fit parameters from seven to six, the precision of V_{Tp} values was improved without

Table 3. Model fit and model comparison.

Volume of interest	Akaike information criterion				F-value		% of regions with better fits than 2TDI[k_4]‡	
	2TSI[k_4]	2TDI	2TDI[k_4]	1TDI	2TDI vs. 2TDI[k_4]*	2TDI vs. 1TDI†	2TDI[k_4]	1TDI
Frontal cortex	19.7 (8.5–45.1)	5.0 (−23.1–21.5)	6.0 (−23.7–38.7)	21.4 (−3.9–50.7)	3.0 (−3.1–13.8)	15.3 (−0.4–78.7)	70.0	20.0
Parietal cortex	18.7 (−3.8–58.8)	−0.1 (−33.5–66.9)	14.5 (−9.4–53.4)	27.7 (3.9–63.3)	0.23 (−4.8–138.4)	14.4 (1.9–94.4)	70.0	10.0
Temporal cortex	15.1 (−22.7–53.3)	2.1 (1.8–72.7)	7.9 (−15.7–55.4)	18.1 (−8.2–57.2)	1.3 (−4.6–17.2)	10.8 (−0.8–41.9)	60.0	30.0
Caudate	30.0 (21.4–38.9)	32.9 (13.3–46.7)	32.5 (12.5–59.2)	31.3 (16.5–50.2)	0.12 (−5.0–2.8)	2.8 (−2.2–43.4)	90.0	60.0
Putamen	33.0 (18.9–62.3)	31.0 (0.9–68.6)	32.5 (2.7–51.8)	38.6 (26.4–60.7)	0.0 (−6.2–5.0)	4.6 (0.24–32.7)	90.0	50.0
Thalamus	28.5 (13.5–64.1)	28.0 (1.8–72.7)	18.4 (−1.1–70.5)	32.2 (8.5–67.6)	1.7 (−8.4–6.4)	2.1 (−2.6–46.5)	90.0	60.0
Brainstem	16.0 (−1.2–30.2)	13.4 (−18.0–48.6)	12.8 (−16.8–29.1)	18.4 (−2.5–38.5)	0.11 (−9.5–7.5)	5.6 (−4.5–69.3)	80.0	50.0
Cerebellar cortex	20.7 (−13.1–68.9)	31.9 (−12.1–74.2)	17.8 (−14.9–75.1)	23.2 (−10.2–72.2)	0.31 (−2.4–5.5)	6.5 (1.4–17.4)	90.0	50.0

Data of healthy volunteers (n = 10) are presented as median and range. The tabulated value for F statistics at a p-level of 0.05 is *4.60 and †3.74, respectively. ‡refers to the F-test. 2TSI[k_4]: two tissue compartment model with single input function and fixed k_4; 2TDI: two tissue compartment model with dual input function; 2TDI[k_4]: two tissue compartment model with dual input function and fixed k_4; 1TDI: one tissue compartment model with dual input function.

significantly increasing the residual variation of the fit and by yielding highly correlated V_{Tp} estimates. Although a further reduction of the parameters by using the one tissue compartment model resulted in slightly more stable outcome measures, the model fit deteriorated (as indicated by AIC and F-test). Furthermore, 1TDI underestimates the radioligand's V_{Tp}. The overall small V_{Tp} of dual input models seems to be related to a high plasma protein binding of [^{11}C]SMW139 (97.2 ± 1.1%), since a low K_{1p}/k_{2p} ratio (Supplemental Table 3) is usually caused by high affinity to plasma proteins. It is also noteworthy that the combination of two metabolites into one input and one tissue metabolite compartment violates the concept of compartment and might impair the model fit to a certain degree. However, modeling with three input functions (by separating K_{1m} and k_{2m} for both radiometabolites) would – although theoretically more precise – require two additional fitting parameters and therefore be less feasible.

Taken together, the 2TDI[k_4] can be recommended as the preferred model for P2X$_7$R quantification with [^{11}C]SMW139, though the benefit of adding stability due to fixing k_4 must be confirmed in the respective patient population. The estimation of k_4 is weighted on late time points of the scan and therefore particularly hampered by the observed tracer kinetics with increasing TACs due to brain-penetrant radiometabolites. We initially expected that the consideration of radiometabolites would improve the stability of k_4 such that the added benefit of fixing k_4 is negligible. The combination of low non-displaceable distribution volume and low levels of target expression, however, might not only lead to small V_{Tp}, but also hamper the stable estimation of "true" k_4. Therefore, adding stability due to reducing the parameters to fit might outweigh variability of k_4 in healthy subjects and patients with subtle neuroinflammatory abnormalities,[4,23] but a strong inflammatory response accompanied by local heterogeneity of the brain tissue [26] due to microglia activation may result in a more pronounced variability of k_4.

Some limitations of this study need to be mentioned. Due to their earlier Rt than the parent tracer in radioHPLC (i.e. greater hydrophilicity), the metabolites are more polar than the parent tracer, and thus, they have a less pronounced ability to cross the BBB. The study does not reveal if radiometabolite 1 crosses the BBB or is metabolized within the brain. To our knowledge, the structure of these radiometabolites is unknown and separate studies are needed to identify the radiometabolites and evaluate the route of metabolism of [^{11}C]SMW139.[27] The radioHPLC analysis of the plasma samples indicates that the metabolism of [^{11}C]SMW139 in mice was faster than the metabolism in human subjects. Therefore, it is reasonable to
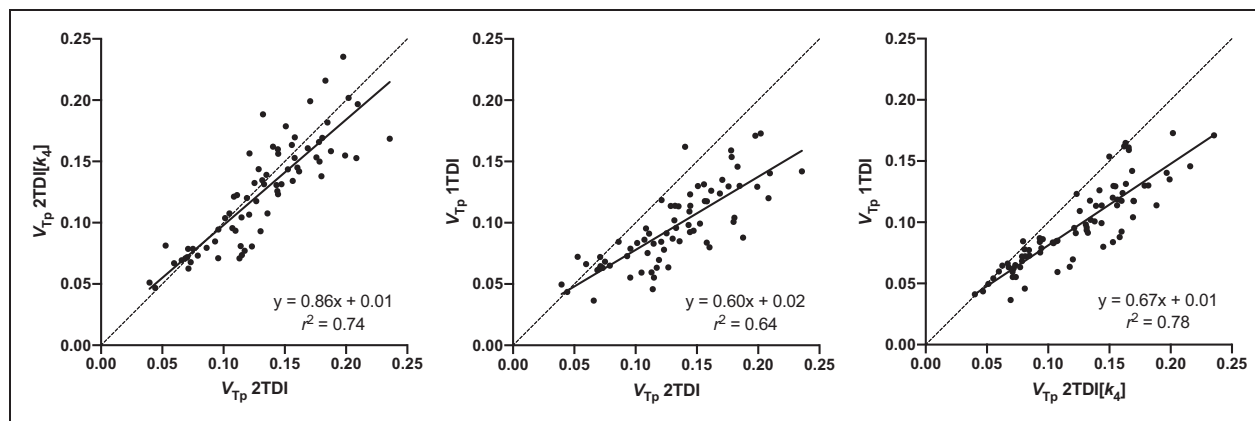
Figure 4. Scatter plots and linear regression analysis. Distribution volume estimates of unchanged [^{11}C]SMW139 (V_{Tp}) within all evaluated brain regions obtained with three models using dual input function: two tissue compartment model (2TDI), two tissue compartment model with a dual run procedure and fixed k_4 (2TDI[k_4]), and one tissue compartment model (1TDI).

assume that the accumulation rates of radiometabolites 1 and 3 in the human brain are low and might not represent major confounders in this study. The determination of the exact radiometabolite fractions in human subjects was also affected by the low radioactivity concentrations of the samples collected at later time points causing a low signal-to-noise ratio in the radioHPLC analysis. The uncertainty in the estimation of the radiometabolite fractions might have contributed to some variability. However, the kinetic analysis performed using all the plasma radiometabolite fractions (including radiometabolite 2) provided similar results (data not shown), suggesting that the exact determination of the individual fractions did not affect the results to a large extent.

The homogeneous cohort of participants and the combination of data from two study sites with minor methodological differences (see also Supplemental Table 1 and Supplemental Figure 1), make the results fairly generalizable. However, further validation work is required for [^{11}C]SMW139 PET. In particular, the model comparison should be validated in patient populations or with an inflammation model in healthy humans or nonhuman primates.[28,29] In presence of a strong neuroinflammatory response, a simplified pseudo-reference approach for [^{11}C]SMW139 is imaginable, assuming no specific binding of the radiometabolites to the P2X$_7$R and thus, a similar amount of metabolites in the target and pseudo-reference region. Recent studies with the P2X$_7$R radioligand [^{11}C] JNJ54173717 did not report an increase of P2X$_7$R in patients with Parkinson's disease or amyotrophic lateral sclerosis.[30,31] Additional work is ongoing to measure P2X$_7$R availability in neurodegenerative disorders using [^{11}C]SMW139.

In conclusion, the quantification of the binding of [^{11}C]SMW139 to human P2X$_7$R is greatly enhanced by using a dual input function model, with the assumption of a similar path of metabolism and BBB penetration ability of radiometabolites in mice and humans. In this cohort of ten healthy volunteers, kinetic modeling with plasma parent and radiometabolite input function allowed robust estimation of [^{11}C]SMW139 distribution volumes with low variability.

Declaration of conflicting interests

The author(s) declared the following potential conflicts of interest with respect to the research, authorship, and/or publication of this article: All authors report no conflict of interest.

Authors' contributions

JB: study design, data analysis, data interpretation, writing; RA: study design, data acquisition, data analysis, data interpretation, writing; AF: data analysis, data interpretation, revising the manuscript; PM: data acquisition, data analysis, revising the manuscript; VK, SW: data acquisition, revising the manuscript; MMM: data acquisition, data analysis, writing; SN: data acquisition, writing; MK, ADW, CH, MHS, PF: study design, data interpretation, revising the manuscript; VO: data analysis, data interpretation, revising the manuscript; JOR: study design, data acquisition, data interpretation, revising the manuscript; AV: study design, data

acquisition, data interpretation, writing. All authors read and approved the final manuscript.

ORCID iDs

Joachim Brumberg (iD) https://orcid.org/0000-0003-0959-4776
Richard Aarnio (iD) https://orcid.org/0000-0002-6420-514X

Supplemental material

Supplemental material for this article is available online.

References

1. Laurent C, Buee L and Blum D. Tau and neuroinflammation: what impact for Alzheimer's disease and tauopathies? *Biomed J* 2018; 41: 21–33.
2. Refolo V and Stefanova N. Neuroinflammation and glial phenotypic changes in alpha-synucleinopathies. *Front Cell Neurosci* 2019; 13: 263.
3. Hickman S, Izzy S, Sen P, et al. Microglia in neurodegeneration. *Nat Neurosci* 2018; 21: 1359–1369.
4. Jacobs AH and Tavitian B. Noninvasive molecular imaging of neuroinflammation. *J Cereb Blood Flow Metab* 2012; 32: 1393–1415.
5. Perry VH, Nicoll JA and Holmes C. Microglia in neurodegenerative disease. *Nat Rev Neurol* 2010; 6: 193–201.
6. Monif M, Burnstock G and Williams DA. Microglia: proliferation and activation driven by the P2X7 receptor. *Int J Biochem Cell Biol* 2010; 42: 1753–1756.
7. Inoue K and Tsuda M. Purinergic systems, neuropathic pain and the role of microglia. *Exp Neurol* 2012; 234: 293–301.
8. Jiang LH, Baldwin JM, Roger S, et al. Insights into the molecular mechanisms underlying mammalian P2X7 receptor functions and contributions in diseases, revealed by structural modeling and single nucleotide polymorphisms. *Front Pharmacol* 2013; 4: 55.
9. Mesuret G, Engel T, Hessel EV, et al. P2X7 receptor inhibition interrupts the progression of seizures in immature rats and reduces hippocampal damage. *CNS Neurosci Ther* 2014; 20: 556–564.
10. Janssen B, Vugts DJ, Wilkinson SM, et al. Identification of the allosteric P2X7 receptor antagonist [(11)C] SMW139 as a PET tracer of microglial activation. *Sci Rep* 2018; 8: 6580.
11. Beaino W, Janssen B, Kooijman E, et al. PET imaging of P2X7R in the experimental autoimmune encephalomyelitis model of multiple sclerosis using [(11)C]SMW139. *J Neuroinflammation* 2020; 17: 300.
12. Hagens MHJ, Golla SSV, Janssen B, et al. The P2X7 receptor tracer [(11)C]SMW139 as an in vivo marker of neuroinflammation in multiple sclerosis: a first-in man study. *Eur J Nucl Med Mol Imaging* 2020; 47: 379–389.
13. Andersson J, Truong P and Halldin C. In-target produced [11C]methane: Increased specific radioactivity. *Appl Radiat Isot* 2009; 67: 106–110.
14. Aarnio R, Alzghool OM, Wahlroos S, et al. Novel plasma protein binding analysis method for a PET tracer and its radiometabolites: a case study with [(11) C]SMW139 to explain the high uptake of

radiometabolites in mouse brain. *J Pharm Biomed Anal* 2022; 219: 114860.
15. Schain M, Toth M, Cselenyi Z, et al. Improved mapping and quantification of serotonin transporter availability in the human brainstem with the HRRT. *Eur J Nucl Med Mol Imaging* 2013; 40: 228–237.
16. Fischl B, Salat DH, Busa E, et al. Whole brain segmentation: automated labeling of neuroanatomical structures in the human brain. *Neuron* 2002; 33: 341–355.
17. Moein MM, Nakao R, Amini N, et al. Sample preparation techniques for radiometabolite analysis of positron emission tomography radioligands; trends, progress, limitations and future prospects. *Trac Trend Anal Chem* 2019; 110: 1–7.
18. Moein MM, Toth M, Tari L, et al. New approach in radiometabolite analysis of positron emission tomography (PET) radioligands; lead-shielded microextraction by packed sorbent as a tool for in vivo radiometabolite analysis of [(11)C]SMW139 in rat plasma. *Talanta* 2020; 208: 120449.
19. Jucaite A, Svenningsson P, Rinne JO, et al. Effect of the myeloperoxidase inhibitor AZD3241 on microglia: a PET study in Parkinson's disease. *Brain* 2015; 138: 2687–2700.
20. Fujita M, Seibyl JP, Verhoeff NP, et al. Kinetic and equilibrium analyses of [(123)I]epidepride binding to striatal and extrastriatal dopamine D(2) receptors. *Synapse* 1999; 34: 290–304.
21. Innis RB, Cunningham VJ, Delforge J, et al. Consensus nomenclature for in vivo imaging of reversibly binding radioligands. *J Cereb Blood Flow Metab* 2007; 27: 1533–1539.
22. Akaike H. New look at statistical-model identification. *Ieee Trans Automat Contr* 1974; 19: 716–723. Ac19:
23. Berdyyeva T, Xia C, Taylor N, et al. PET imaging of the P2X7 ion channel with a novel tracer [(18)F]JNJ-64413739 in a rat model of neuroinflammation. *Mol Imaging Biol* 2019; 21: 871–878.
24. Hashimoto H, Kawamura K, Igarashi N, et al. Radiosynthesis, photoisomerization, biodistribution, and metabolite analysis of 11C-PBB3 as a clinically useful PET probe for imaging of tau pathology. *J Nucl Med* 2014; 55: 1532–1538.
25. Maruyama M, Shimada H, Suhara T, et al. Imaging of tau pathology in a tauopathy mouse model and in alzheimer patients compared to normal controls. *Neuron* 2013; 79: 1094–1108.
26. Delforge J, Syrota A and Bendriem B. Concept of reaction volume in the in vivo ligand-receptor model. *J Nucl Med* 1996; 37: 118–125.
27. Osman S, Lundkvist C, Pike VW, et al. Characterisation of the appearance of radioactive metabolites in monkey and human plasma from the 5-HT1A receptor radioligand, [carbonyl-11C]WAY-100635 – explanation of high signal contrast in PET and an aid to biomathematical modelling. *Nucl Med Biol* 1998; 25: 215–223.
28. Hannestad J, Gallezot JD, Schafbauer T, et al. Endotoxin-induced systemic inflammation activates microglia: [(1)(1)C]PBR28 positron emission tomography in nonhuman primates. *Neuroimage* 2012; 63: 232–239.

29. Sandiego CM, Gallezot JD, Pittman B, et al. Imaging robust microglial activation after lipopolysaccharide administration in humans with PET. *Proc Natl Acad Sci U S A* 2015; 112: 12468–12473.

30. Van Weehaeghe D, Koole M, Schmidt ME, et al. [11C]JNJ54173717, a novel P2X7 receptor radioligand as marker for neuroinflammation: human biodistribution, dosimetry, brain kinetic modelling and quantification of brain P2X7 receptors in patients with Parkinson's disease and healthy volunteers. *Eur J Nucl Med Mol Imaging* 2019; 46: 2051–2064.

31. Van Weehaeghe D, Van Schoor E, De Vocht J, et al. TSPO versus P2X7 as a target for neuroinflammation: an *in vitro* and *in vivo* study. *J Nucl Med* 2020; 61: 604–607.